Geomorphology 327 (2019) 438–445

Contents lists available at ScienceDirect

Geomorphology

journal homepage: www.elsevier.com/locate/geomorph

Episodic erosion in West Antarctica inferred from cosmogenic ^{3}He and ^{10}Be in olivine from Mount Hampton

A. Carracedo [a,*], Á. Rodés [a], J.L. Smellie [b], F.M. Stuart [a]

[a] Isotope Geosciences Unit, Scottish Universities Environmental Research Centre, Rankine Avenue, East Kilbride G75 0QF, UK
[b] Department of Geology, University of Leicester, UK

ARTICLE INFO

Article history:
Received 30 August 2018
Received in revised form 19 November 2018
Accepted 19 November 2018
Available online 22 November 2018

Keywords:
Cosmogenic nuclides (^{3}He, ^{10}Be)
Olivine
Erosion rates
Episodic erosion
Mount Hampton
West Antarctica

ABSTRACT

The polar climate of Antarctica results in the lowest erosion rates on Earth. The low long-term erosion history of high elevation mountain tops that are exposed above the ice preserve a record of climate change that can be accessed using cosmogenic nuclides. However, unravelling the complexity of the long-term denudation histories of Antarctic summits is frequently hampered by intermittent ice cover. The aim of this work is to identify denudation rate changes in a surface that has been continuously exposed since the middle Miocene. We have measured stable (^{3}He) and radioactive (^{10}Be) cosmogenic nuclides in olivine from lherzolite xenoliths from the summit of the Mount Hampton shield volcano within the West Antarctic Ice Sheet. The peak (3200 m) has never been covered by the current ice sheet and local ice caps, consequently the data record the subaerial erosion history of a mountain top within the Antarctic interior. The ^{10}Be concentrations in the olivines yield minimum exposure ages (33 to 501 ka) that are significantly younger than those derived from the cosmogenic ^{3}He (90 to 1101 ka). The data reveal a complex exposure history that provide an integrated long-term erosion rate of between 0.2 and 0.7 m/My that is most likely caused by mechanical weathering. Inverse modelling shows that the data are readily explained by episodic erosion, consisting of one to five erosion pulses that may record major regional climatic changes.

© 2018 Elsevier B.V. All rights reserved.

1. Introduction

To understand long-term landscape evolution and the role played by Cenozoic climate change, it is essential to quantify the rates of erosion over different timescales (Peizhen et al., 2001). The high elevation mountain tops in Antarctica have been exposed over many successive glacial-interglacial cycles and are sensitive to the changing climatic conditions (Sugden et al., 2005). Antarctica is the highest, driest, coldest and windiest continent and records some of the lowest denudation rates (e.g., Margerison et al., 2005) comparable only to the driest deserts, e.g., Atacama (Placzek et al., 2010) and South Africa (Kounov et al., 2007). Consequently, the erosional record of the high altitude surfaces has the potential to record climatic variations over millions of years. Although climate changes affect the rate of landscape evolution, in most cases the changes are averaged out into apparent steady-state erosion rates preventing identification of the intrinsic dynamics of the landscape (Brunsden and Thornes, 1979). Combining stable and radioactive cosmogenic nuclides has proved to be a useful method to determine the complexity of landscape evolution (Balco and Shuster, 2009).

Most studies of high elevation Antarctic landscapes have combined ^{21}Ne, ^{10}Be, and ^{26}Al in quartz-bearing surfaces (Van der Wateren et al., 1999; Oberholzer et al., 2003; Di Nicola et al., 2009, 2012; Middleton et al., 2012; Mukhopadhyay et al., 2012). They typically identify complex exposure histories that are frequently interpreted to record intermittent burial beneath ice (e.g., Nishiizumi et al., 1991; Di Nicola et al., 2009, 2012; Mukhopadhyay et al., 2012; Hein et al., 2016; Sugden et al., 2017). In these cases erosion is assumed to be in steady state, implying equilibrium between the nuclides produced by cosmic radiation near the surface and the nuclide loss caused by constant-surface erosion rate (Lal, 1991). Middleton et al. (2012) demonstrated how ^{26}Al-^{10}Be-^{21}Ne data from potholes in the Dry Valleys, East Antarctica record changes in erosion rate rather than burial underneath ice.

Currently, ice-free regions comprise only a few percent of the Antarctic continent, and, of those, only a small proportion has been ice-free since the Miocene (Ackert et al., 1999; Stone et al., 2003; Mukhopadhyay et al., 2012). The high elevation peaks (>3 km) in the Marie Byrd Land in West Antarctica are permanently exposed regions where wind-induced ablation is more rapid than snow accumulation (Nicolas and Bromwich, 2014). As such, they are a key natural laboratory for the study of the erosional history of the Antarctic interior.

In the first study of its kind we have developed cosmogenic ^{10}Be determination in olivines and combined new data with cosmogenic

* Corresponding author.
E-mail address: Fin.Stuart@glasgow.ac.uk (A. Carracedo).

https://doi.org/10.1016/j.geomorph.2018.11.019
0169-555X/© 2018 Elsevier B.V. All rights reserved.

^{3}He measurements on the same samples to unravel the erosional history of the summit of the Mount Hampton volcano within the West Antarctic ice sheet (WAIS). The edifice has never been covered by a significant thickness of ice and, thus, provides a simple test of the regional erosional history under hyperarid climatic conditions (Rocchi et al., 2006). The data reveal a complex erosional history that requires long periods of extremely low erosion interspersed with periods of more rapid erosion that may reflect the influence of climate variations on the mechanical subaerial erosion.

2. Geological and glaciological context

Mount Hampton is the northern-most volcano of 18 that protrude through the WAIS in the Executive Committee Range (ECR) on the uplifted northern flank of the West Antarctic Rift (Fig. 1). It is one of the oldest volcanoes in Marie Byrd Land, likely produced during a peak of volcanism in the late Miocene (13.4 to 8.6 Ma; LeMasurier and Rex, 1989; LeMasurier and Thomson, 1990). The summit (3323 m asl) is ~1000 m above the current WAIS surface and shows no evidence of significant erosional dissection. The edifice is a symmetrical, well-preserved shield volcano with 10–15° constructional slopes dominantly composed of feldspar- and augite-phyric phonolite lavas (LeMasurier, 1987; LeMasurier and Thomson, 1990; LeMasurier and Rocchi, 2005; Rocchi et al., 2006). Crustal and lithospheric mantle xenoliths, including a suite of spinel-bearing lherzolites, are found within basanites that were erupted as parasitic cones close to the volcano summit (LeMasurier and Kawachi, 1990).

The surface elevation of the WAIS was at its highest at around 10 ka (Ackert et al., 1999, 2007; Anderson et al., 2002; Stone et al., 2003). The O and H isotope composition of the Byrd ice core records ice elevations that were 400 to 500 m above the current ice level during the Last Glacial Maximum (LGM) and early Holocene (Steig et al., 2001). Cosmogenic ^{3}He and ^{36}Cl ages of moraines from Mount Waesche in the ECR suggest that the WAIS has expanded vertically just ~45 m since the LGM (Ackert et al., 1999). The ^{10}Be exposure ages of glacially transported cobbles from the Ford Ranges in Marie Byrd Land suggest that during the LGM the WAIS was ~700 m higher than today near the coast and ~200 m higher in the interior (Stone et al., 2003). A more recent study using cosmogenic ^{21}Ne and ^{10}Be from nunataks in the Ohio Range on the boundary between West and East Antarctica suggest that ice thickness has not been >160 m above current ice levels (~2200 m) since the late Miocene (~7 Ma) (Mukhopadhyay et al., 2012). All studies undertaken so far indicate that the highest volcanic peaks of the ECR (>3000 m) have been above the ice sheet surface since their eruption in the late Miocene (Ackert et al., 1999; Stone et al., 2003; Mukhopadhyay et al., 2012).

3. Sample description

We have analysed seven lherzolite xenoliths collected from a boulder field near the summit of Mount Hampton (76°30 S 125°52 W) during the second season of the Antarctic expedition WAVE (West Antarctic Volcano Exploration) in January 1991. The xenoliths are 4 to 8 cm diameter and were collected from within a few meters of each other on the western flank. They are all likely products from the same parasitic cone eruption that occurred at around 11.4 Ma (LeMasurier and Rex, 1989). The xenoliths are typically composed of >50% olivine (>250 μm), ~35% orthopyroxene (>250 μm), ~10% clinopyroxene (200 to 500 μm), and <2% spinel (<200 μm) (Wysoczanski et al., 1995; LeMasurier et al., 2003). Electron microprobe analysis (this study) reveals that the olivines from each xenolith have a near constant chemical composition around Fo_{90} and no significant compositional zonation.

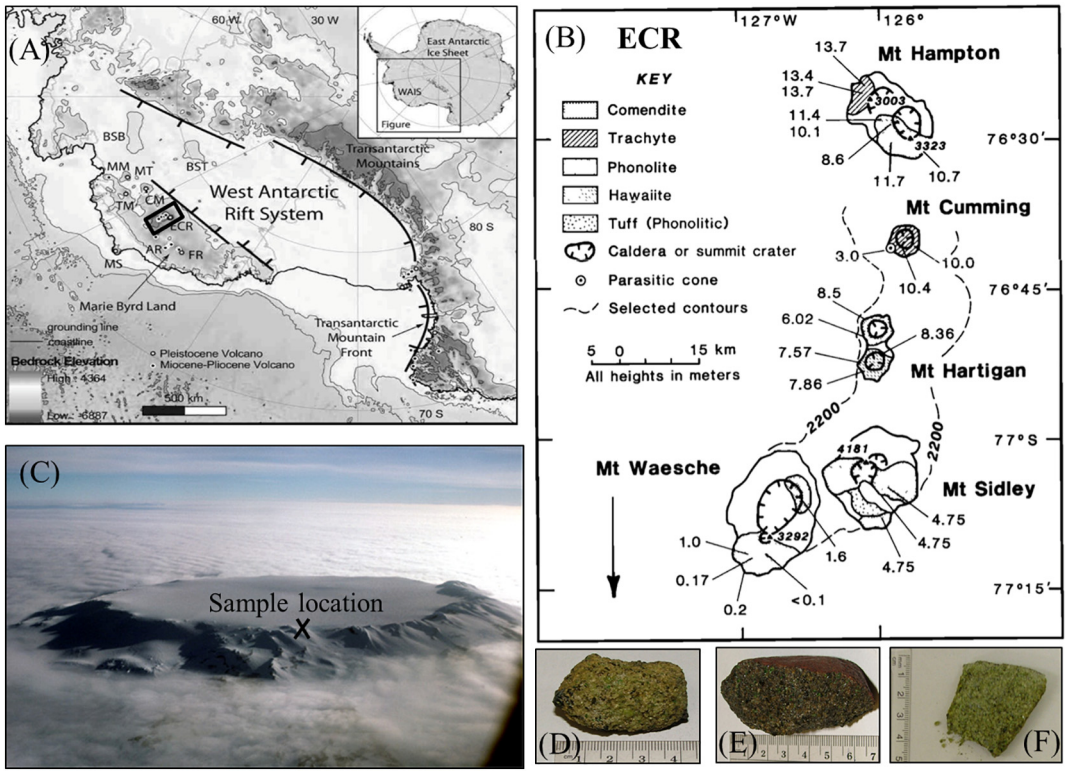

Fig. 1. (**A**) Elevation map of Antarctica showing the location of the Executive Committee Range (ECR) within Marie Byrd Land in the West Antarctic Ice Sheet interior (modified from Paulsen and Wilson, 2010). The black box represents the map in (B). (**B**) Geologic map of the ECR showing K—Ar ages and the sample location. This figure is modified from LeMasurier and Rex (1989). (**C**) Aerial view of Mount Hampton showing the sampling area for the xenoliths analysed in this study. Photograph: John Smellie. Representative xenolith samples are MH.1 (D), MH.2 (E), and MB.71.8 (F).

4. Analysis procedures

4.1. Helium isotope determinations

The xenoliths were gently crushed, and unaltered mineral inclusion-free olivine grains were handpicked from the 250–500 μm fraction under a binocular microscope. This fraction was then cleaned in pure acetone (≥99.8%) and ~15 mg aliquots were encapsulated in Pt tubes and loaded in 21-hole Cu pans. Each sample was degassed at ~1400 °C using a 75 W 808 nm diode laser (Foeken et al., 2006). The magmatic helium contribution was determined on ~1 g of olivine from xenolith MH.1 by analysis of the gas released by in vacuo crushing using a multisample hydraulic crusher following procedures in Stuart et al. (2003).

Helium concentrations and isotope compositions were measured using a *ThermoFisher* Helix SFT mass spectrometer at Scottish Universities Environmental Research Centre. The instrument was tuned to the maximum sensitivity following procedures recommended by Burnard and Farley (2000) and Mabry et al. (2012). The instrument source was operated at 4.5 kV to produce resolution >700, reduce beam dispersion, and provide the best peak shape and sensitivity (Mabry et al., 2012). The average static background levels of the instrument are $1.98 \pm 0.19 \times 10^8$ and $5.0 \pm 1.9 \times 10^3$ atoms of ^{4}He and ^{3}He respectively. Repeated analysis of 3×10^{12} atoms of ^{4}He and 9×10^7 atoms of ^{3}He of the HESJ standard (Matsuda et al., 2002) revealed a reproducibility of 0.2% and 1.1% for ^{4}He and ^{3}He measurements respectively.

4.2. ^{10}Be determinations

Beryllium-10 was extracted and analysed from ~1 g of olivine. Meteoric ^{10}Be was removed by three sequential HF and HCl dissolutions, that etched out >25% of the initial mass. The remaining olivine was dissolved in HF and spiked with ~500 μg of ^{9}Be carrier (Bourlès, 1988; Brown et al., 1992). As the samples contained high amounts of Mg and Fe, a procedure for isolation of Be was developed. First, a bulk Be separation was performed by solvent extraction using acetyl acetone at neutral pH in the presence of ethylenediaminetetra-acetic acid (EDTA) (Tabushi, 1958; Seidl, 1993; Seidl et al., 1997). Beryllium was then extracted and separated by ion chromatography and precipitated as BeOH using routine procedures (e.g. Child et al., 2000). The precipitate was then oxidized at 800 °C, mixed with 6 parts of Nb, and pressed into a Cu cathode. The procedure is summarized in Fig. 2. The ^{10}Be/^{9}Be ratios of the six samples and the blank were measured using the 5 MV NEC Pelletron accelerator mass spectrometer at SUERC (Xu et al., 2010). The ^{10}Be concentrations are based on a ^{10}Be/^{9}Be ratio of 2.79×10^{-11} for NIST Standard Reference Material 4325. The data have been corrected with a procedural blank (representing 0.4 to 6% of the total ^{10}Be measured).

4.3. Production rates

The production rates used for exposure age and erosion rate calculations from the measured cosmogenic ^{3}He and ^{10}Be concentrations are scaled for latitude (76°30′S, 125°52′W) and elevation (3020 m) using Lal (1991)/Stone (2000) scaling factors and following the scheme implemented by Balco et al. (2008) for ^{10}Be and Marrero et al. (2016) for ^{3}He. The SLHL production rate for ^{3}He is taken from Goehring et al. (2010) and ^{10}Be is taken from Borchers et al. (2016). The production rates are scaled for composition using production ratios obtained from the element-specific production rates of Masarik (2002). To calculate the theoretical erosion rates, we applied inverse modelling using a convergent Monte-Carlo approach based on the equations from Lal (1991), detailed explanation of the calculations, and parameters used for modelling are provided in Section 6.2.

5. Results

The ^{3}He concentrations and ^{3}He/^{4}He ratios are reported in Table 1. The ^{3}He concentrations in the melt steps vary from 1.5 to 18.9×10^8 atoms/g and ^{3}He/^{4}He ratios range from 24 to 11,543 R_a, where R_a is the isotope composition of He in air (1.39×10^{-6}). Multiple aliquots of olivine from each xenolith were measured. Helium was measured in nine aliquots of olivine from xenolith MH.2 in an effort to fully determine the data quality. The ±5% uncertainty in the average ^{3}He concentration is beyond the reproducibility determined from HESJ. This overdispersion is unlikely to represent variation in other He sources (see below) and may reflect weighing errors and subtle variation in cosmogenic He production within the xenolith.

Determining the cosmogenic He concentration in old volcanic rocks requires that the inventories of nucleogenic-radiogenic and magmatic

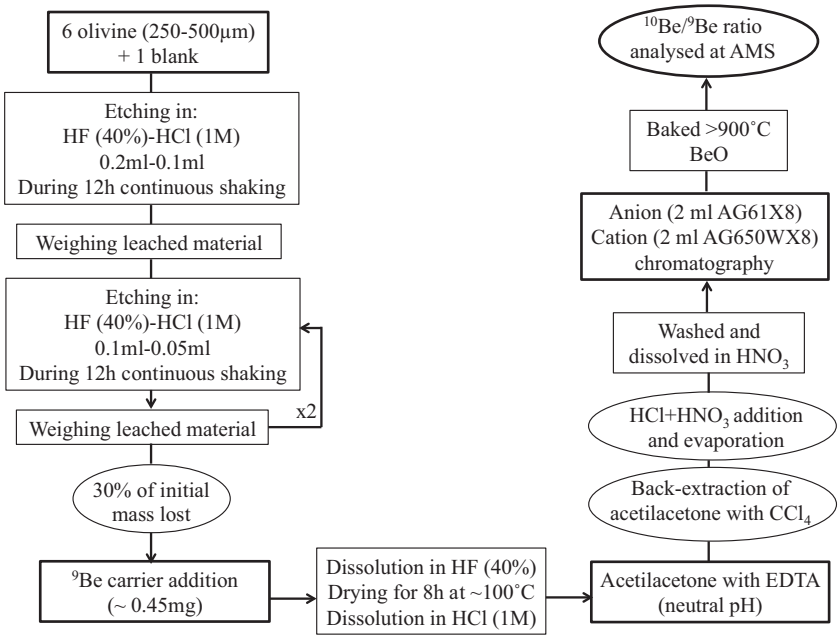

Fig. 2. Schematic representation of the procedures followed for ^{10}Be isolation from olivine.

Table 1
Helium isotope data from olivine separates from Mount Hampton xenoliths.

Sample	Weight (mg)	^{3}He (10^8 atoms/g)	1σ	^{3}He/^{4}He (R_a)	1σ
MH.1	9.7	15.77	0.19	8429	198
MH.1	11.2	15.73	0.19	1525	1
Average		15.75	0.03		
MH.2	12.0	8.43	0.14	211	4
MH.2	13.5	8.27	0.15	1469	33
MH.2	12.1	7.44	0.12	5849	156
MH.2	14.0	7.96	0.11	4902	101
MH.2	12.2	7.68	0.13	5001	157
MH.2	14.9	7.62	0.12	10,693	245
MH.2	15.0	7.65	0.12	11,543	279
MH.2	11.3	8.52	0.15	3523	56
MH.2	16.6	7.91	0.13	2330	48
Average		7.94	0.39		
MB.71.7	13.7	1.79	0.05	24	1
MB.71.7	9.5	1.77	0.06	134	5
Average		1.78	0.01		
MB.71.8	12.3	18.94	0.21	2524	345
MB.71.8	16.4	18.67	0.19	1126	18
Average		18.81	0.19		
MB.71.9	18.0	5.26	0.09	432	9
MB.71.9	12.9	5.13	0.08	543	11
MB.71.9	14.9	5.68	0.09	396	8
MB.71.9	12.4	5.40	0.11	174	4
Average		5.37	0.24		
MB.71.10	13.4	1.56	0.05	783	30
MB.71.10	8.0	1.53	0.06	35	2
MB.71.10	12.6	1.47	0.04	63	2
MB.71.10	10.6	1.46	0.04	449	14
Average		1.51	0.05		

He are quantified (Margerison et al., 2005; Williams et al., 2005). The ^{3}He/^{4}He ratio of nucleogenic-radiogenic He produced in olivine is low, approaching the canonical value of crustal radiogenic He (<0.05 R_a), reflecting the low Li content (Ryan and Kyle, 2004; Seitz et al., 2004). The high measured ^{3}He/^{4}He ratios of the Mount Hampton olivines (>24 R_a) imply that the contribution of nucleogenic ^{3}He is negligible.

In vacuo crushing extracts magmatic He by rupturing melt/vapour inclusions (e.g., Stuart et al., 1995). Sample MH.1 released 2.8 ± 0.8 × 10^5 atoms ^{3}He/g, yielding a ^{3}He/^{4}He ratio of 9.02 ± 1.64 R_a (1σ). Panter et al. (2000) characterized the basalts from the Marie Byrd Land as having a strong high μ (HIMU) signature with no evidence of crustal contamination. If the ^{3}He/^{4}He ratio of HIMU-influenced mantle is 6.5 ± 0.6 R_a (Parai et al., 2009, and references therein), a small contribution of cosmogenic He has been released by crushing. The cosmogenic ^{3}He released by crushing (8.2 ± 4.1 × 10^4 atoms/g) represents <0.05% of the total of the sample with least $^3He_{cos}$ (see below), demonstrating that the in vacuo crushing method employed here does not release a significant proportion of the cosmogenic ^{3}He in olivine.

The concentration of magmatic ^{3}He ($^3He_{magmatic}$) released by crushing can be calculated from the following relationship:

$$^3He_{magmatic} = {}^3He_{crush} \times \left({}^3He/{}^4He_{magmatic}/{}^3He/{}^4He_{crush}\right) \quad (1)$$

where the subscript crush refers to He released by in vacuo crushing. The magmatic ^{3}He released in this experiment (1.98 × 10^5 atoms/g) represents <0.1% of the total ^{3}He released by melting the Mount Hampton olivines. Thus, it can be neglected, implying that all the ^{3}He released by degassing all samples can be considered to be cosmogenic in origin.

The minimum exposure ages calculated from the average cosmogenic ^{3}He concentrations in each sample range from 90 to 1101 ka (Table 2). These correspond to steady-state erosion rates of 0.45 to 5.51 m/Ma (Table 2).

The ^{10}Be concentrations in the Mount Hampton olivines vary from 0.17 to 2.27 × 10^7 atoms/g (Table 2). These correspond to minimum

Table 2
Compilation of the data of ^{10}Be and ^{3}He from olivine separates from xenoliths from Mount Hampton.

Sample	Latitude S	Longitude W	Elevation (m)	Olivine (Fo)	^{10}Be (10^7 atoms/g)	1σ	^{10}Be apparent erosion rate (m/Ma)	1σ	PR ^{10}Be_Qtz scaled with Lal (1991)/ Stone (2000)	N factor	^{10}Be apparent exposure age (ka)	1σ	^{3}He average (10^8 atoms/g)	1σ	^{3}He apparent erosion rate (m/Ma)	1σ	PR ^{3}He_Fo_{84} scaled to Lal (1991)/ Stone (2000)	N factor	^{3}He apparent exposure age (ka)	1σ	^{3}He/^{10}Be	1σ
MH.1	76° 30′	125° 52′	3020	91	2.27	0.04	1.18	0.77	51.92	0.884	501	40	15.75	0.03	0.53	0.08	1674.0289	1.031	925	140	69.43	1.29
MH.2	76° 30′	125° 52′	3020	91	1.01	0.02	3.01	1.75	51.92	0.883	208	16	7.94	0.39	1.05	0.16	1674.0289	1.030	467	74	78.79	3.66
MB.71.7	76° 30′	125° 52′	3020	91	0.17	0.01	19.70	2.49	51.92	0.883	33	3	1.78	0.01	4.70	0.71	1674.0289	1.030	104	16	105.26	5.29
MB.71.8	76° 30′	125° 52′	3020	91	1.76	0.04	1.60	0.99	51.92	0.883	379	30	18.81	0.19	0.45	0.07	1674.0289	1.031	1101	170	106.60	2.47
MB.71.9	76° 30′	125° 52′	3020	89	0.81	0.02	3.85	2.19	51.92	0.875	165	13	5.37	0.24	1.56	0.25	1674.0289	1.029	319	51	66.53	3.38
MB.71.10	76° 30′	125° 52′	3020	90	0.23	0.01	14.68	1.80	51.92	0.877	46	4	1.51	0.05	5.51	0.85	1674.0289	1.030	90	14	67.41	3.52

The scaled production rates of ^{10}Be and ^{3}He are calculated using the CRONUS calculators v. 2.3 (Balco et al., 2008) version 2.3 and Marrero et al. (2016) respectively. The Normalization factor (N) accounts for composition using production ratios obtained from the element-specific production rates of Masarik (2002). Apparent exposure ages are calculated following the equations of Lal (1991), assuming zero erosion.

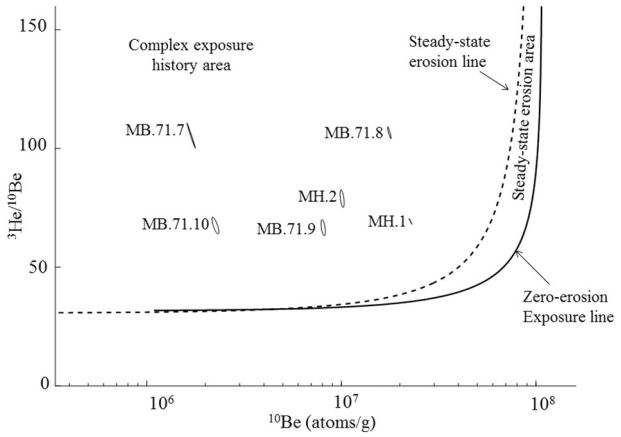

Fig. 3. Plot of ^{10}Be concentration vs. ^{3}He/^{10}Be for Mount Hampton xenolith olivine. Ellipses represent the 68% confidence interval. The banana-shaped area is the steady-state erosion area (Lal, 1991). The continuous line represents the evolution of the ^{3}He/^{10}Be ratio with time in a surface that has experienced zero erosion. The dotted line represents the ^{3}He/^{10}Be ratio generated by steady-state erosion of at least one mean cosmic ray attenuation length at a constant rate for infinite amount of time.

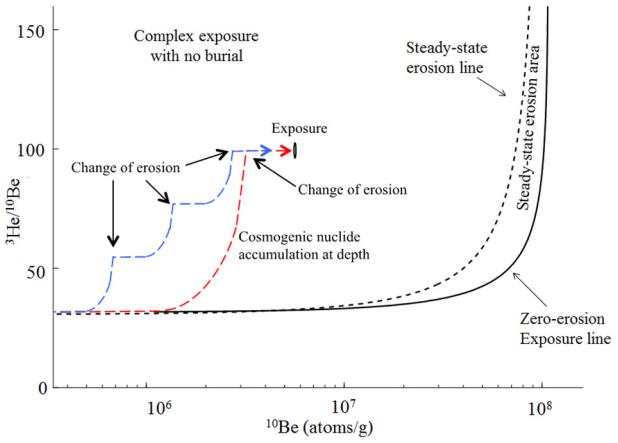

Fig. 4. Schematic representation of the evolution of cosmogenic ^{3}He/^{10}Be ratio under conditions of episodic erosion consisting on several (blue) or one (red) erosion pulses to generate signatures that fall on the complex exposure area of the ^{10}Be vs. ^{3}He/^{10}Be diagram.

exposure ages of between 33 and 501 ka and maximum erosion rates of 1.2 to 19.7 m/Ma (Table 2). The minimum exposure ages are systematically younger than those derived from cosmogenic ^{3}He, and the apparent erosion rates are higher.

The ^{3}He/^{10}Be ratios vary from 66.5 to 106.6. These are more than twice the instantaneous production ratio in olivine (~30). The data plot within the area of complex exposure on a ^{3}He/^{10}Be vs.^{10}Be diagram (Fig. 3) rules out the possibility that they record long-term steady-state erosion. The ^{3}He—^{10}Be data require either a complex history of exposure, burial and reexposure, or pervasive nonsteady state (i.e., variable) erosion (Lal, 1991).

6. Discussion

6.1. Intermittent burial

The Mount Hampton edifice has never been covered by the WAIS (see Section 2), and the summit shows no geomorphic features that are indicative of the accumulation of significant wet-based ice, such as striated, polished, or ice-moulded rock surfaces (LeMasurier, 1987; LeMasurier and Rocchi, 2005; Rocchi et al., 2006). Complete cessation of the production of cosmogenic He and Be requires the local accumulation of ~10 m of cold-based ice. The high elevation and location deep within Marie Byrd Land interior far from coastal areas of high snow precipitation strongly restricts ice accumulation. Marie Byrd Land is the only Antarctic region where the mean katabatic flow has a strong southward component, causing a precipitation shadow effect over the ECR and producing a strong foehn wind effect that causes the snowfall to sublimate/evaporate (Nicolas and Bromwich, 2014). Therefore, it is unlikely that a sizeable ice cap has ever existed for any significant period of time, meaning that intermittent burial caused by a waxing and waning of semipersistent ice cover is implausible.

Volcanic activity at Mount Hampton ceased at 8.6 Ma and migrated southward along the ECR (LeMasurier and Rex, 1989), and no field evidence of tephra deposits near the sample site was observed. This rules out burial beneath intermittent volcanic deposits as an explanation for the ^{3}He—^{10}Be data.

6.2. Erosion rate variation

Lal (1991) noted that nonsteady state erosion, i.e., changing erosion rates, generates cosmogenic nuclide ratios that plot in the complex exposure zone. Kober et al. (2007) and Middleton et al. (2012) also considered the possibility of episodic erosion being the cause of the nonsteady state cosmogenic ^{21}Ne-^{10}Be-^{26}Al signatures in northern Chile and Antarctica respectively. The evolution of the ^{3}He/^{10}Be ratio during nonsteady state erosion is shown in Fig. 4.

To quantify the timescale and magnitude of episodic erosional events and the duration of the final stage of complete exposure that satisfies the Mount Hampton xenolith He—Be data, we have modelled two extreme nonsteady-state erosion scenarios. Model 1 considers multiple erosional pulses that are assumed to last an equal length of time. This is shown schematically in Fig. 5A. In this model the integrated erosion rate is the average over the period since eruption. Model 2 considers the possibility of a single erosion pulse in the Pleistocene that brought all the xenoliths to the surface from different depths. This model assumes that the erosion rate was negligible prior to the erosion pulse and is shown schematically in Fig. 5C. Fig. 5B and D show the evolution of ^{3}He/^{10}Be and ^{10}Be concentrations in the olivines for the two scenarios. Table 3 summarises the parameters and variables used to generate the two models.

Both models start at 11.4 Ma based on the K—Ar age of Mt. Hampton phonolites (LeMasurier and Rex, 1989). The production of cosmogenic ^{3}He and ^{10}Be have been calculated according to

$$^3He = \frac{P_{3sp}}{\frac{\varepsilon\rho}{\Lambda sp}}\left(e^{-\frac{z\rho}{\Lambda sp}}\right)\left(1-e^{-\left(\frac{\varepsilon\rho}{\Lambda sp}\right)T}\right) \quad (2)$$

$$^{10}Be = \frac{P_{10sp}}{\lambda_{10}+\frac{\varepsilon\rho}{\Lambda sp}}\left(e^{-\frac{z\rho}{\Lambda sp}}\right)\left(1-e^{-\left(\lambda 10+\frac{\varepsilon\rho}{\Lambda sp}\right)T}\right)+\frac{P_{10fm}}{\lambda_{10}+\frac{\varepsilon\rho}{\Lambda fm}}\left(e^{-\frac{z\rho}{\Lambda fm}}\right) \times\left(1-e^{-\left(\lambda_{10}+\frac{\varepsilon\rho}{\Lambda fm}\right)T}\right)+\frac{P_{10sm}}{\lambda_{10}+\frac{\varepsilon\rho}{\Lambda sm}}\left(e^{-\frac{z\rho}{\Lambda sm}}\right)\left(1-e^{-\left(\lambda_{10}+\frac{\varepsilon\rho}{\Lambda sm}\right)T}\right) \quad (3)$$

where P_{3sp} and P_{10sp} are the production rates of ^{3}He and ^{10}Be by spallation of fast neutrons; P_{10fm} and P_{10sm} are the ^{10}Be production rates by neutron spallation, fast muon radiation, and negative muon radiation; ε is the erosion rate; ρ is the density of the rock; λ_{10} is the decay constant of ^{10}Be; and $\Lambda_{sp,fm,sm}$ are the respective attenuation lengths with depth z (Lal, 1991; Gosse and Phillips, 2001; Balco et al., 2008). Muon interactions account for nearly all the cosmogenic Be production at a few meters below the surface. Cosmogenic ^{3}He is not produced significantly by muon radiation and is assumed to be negligible in this case.

The models are sensitive to variations in the ^{3}He/^{10}Be ratios rather than in the individual production rates. The effects of self-shielding and from snow cover have been considered. Assuming 1 m of continuous

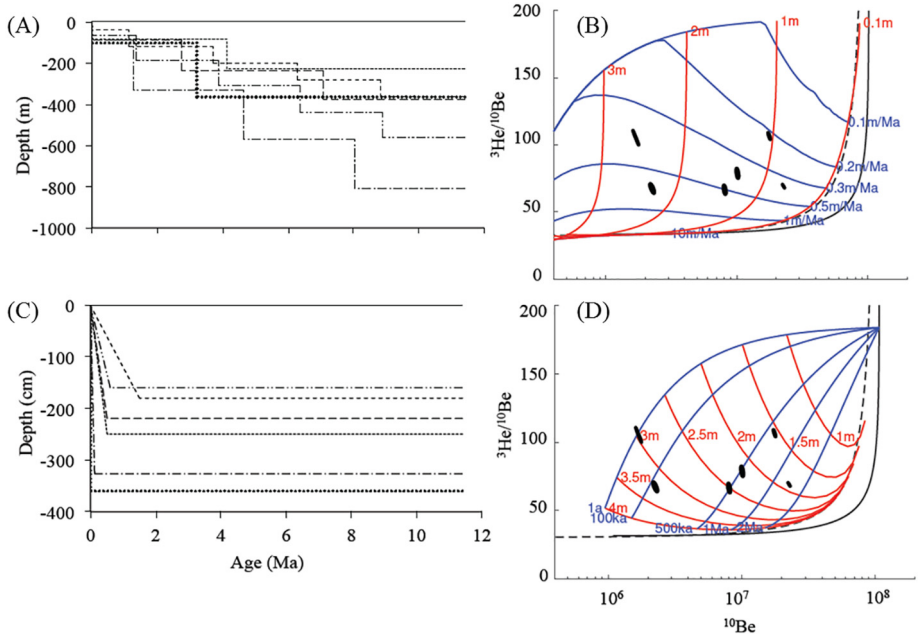

Fig. 5. Two models to explain the cosmogenic ^{3}He and ^{10}Be data from Mount Hampton xenolith olivine. (**A**) and (**C**) are schematic representations of model 1 and model 2 respectively (see text) showing the episodic erosion of several xenoliths (dashed lines) on their way to the surface (continuous line). (**B**) Plot of the output of model 1. The red lines represent the amount of material removed in a single erosional event, and the blue lines record the average erosion rate over 11.4 Ma. The lines have been determined using Eqs. (2) and (3) (see text). The grey continuous and discontinuous lines represent the steady-state erosion area (Lal, 1991; Balco et al., 2008). (**D**) Output of model 2.

snow coverage and an average size of the xenoliths of 4 cm, the ^{3}He/^{10}Be ratios vary by 0.25% having no effect on the interpretation of the models.

The values of the model parameters that fit the sample ^{3}He and ^{10}Be concentrations were calculated by inverse modelling using a convergent Monte-Carlo approach. The parameters that satisfy the pulsed erosion model (model 1) are summarized in Table 4. The data can be explained by between two and five erosion pulses that have removed between 0.8 and 2.6 m of overburden. Thus, the long-term erosion rates range from 0.20 to 0.71 m/My. Erosion rates of this magnitude are typical of high elevation landscapes in the Antarctic (e.g., Marrero et al., 2018, and references therein).

For the single erosional event model (model 2), the minimum depths at which the samples could have resided and the maximum time for the erosion rate change have been determined. Table 5 summarises the results obtained by inverse modelling. The cosmogenic ^{3}He—^{10}Be data require that the xenoliths have spent most of the time since eruption at between 1.6 and 3.0 m below the surface, followed by a pulse of erosion of between 1.2 and 306 m/Ma starting at 1.5 Ma. This model records the maximum amount of material removed in a minimum time with erosion able to remove up to 3.3 m in a short period of time (~10 ka). In this model, the data require a long-term average erosion rate that is <1 m/My.

Table 3
Summary of the parameters used to model the cosmogenic ^{3}He and ^{10}Be data from Mount Hampton xenolith olivine.

Model parameters	Values	Notes and references[a]
General parameters[b]		
^{10}Be production rate for olivine (Fo_{89-91}) at Mount Hampton	45.9 atoms/g/y	Following the scheme of CRONUS calculators Matlab code v 2.3 Balco et al. (2008) scaling factor Lal (1991)/Stone (2000) scaled for composition using Masarik (2002)
^{3}He production in olivine (Fo_{89-91}) at Mount Hampton	1725 atoms/g/y	Following the scheme of Marrero et al. (2016) scaling factor Lal (1991)/Stone (2000) scaled for composition using Masarik (2002)
Production rate from fast muons	0.0777 atoms/g/y	Calculated using CRONUS calculators Matlab code v 2.3 Balco et al. (2008)
Production rate from negative muon capture	0.0992 atoms/g/y	
Attenuation length from neutron spallation	160 g/cm^2	Balco et al. (2008); Gosse and Phillips (2001)
Attenuation length from fast muons	2.60×10^3 g/cm^2	Calculated using CRONUS calculators Matlab code v 2.3 Balco et al. (2008)
Attenuation length from negative muon capture	1.30×10^3 g/cm^3	Calculated using CRONUS calculators Matlab code v 2.3 Balco et al. (2008)
Half-life for ^{10}Be	1.378 Ma	Chmeleff et al. (2010); Korschinek et al. (2010)
Rock density	2.67 g/cm^3	
Constant exposure-erosion lines		Calculated applying equations from Lal (1991) for constant exposure at zero erosion and for steady-state erosion for infinite time
Model 1		Episodic erosion. Material is removed in steps
Average erosion rate (m/Ma)		Erosion rate is taken as an average for the total residence time (11.4 Ma)
Material removed from one erosive event (m)		Erosive events are assumed to last an equal length of time
Total duration of complex history	11.4 Ma	LeMasurier and Rex (1989)
Model 2		Single erosion pulse. Erosion rate is assumed to be zero during the time of accumulation at depth prior to the removal of material
Accumulation depth (m)		Material removed to place the samples at the surface
Time when erosion started		This considers the time at depth required to generate the ^{3}He—^{10}Be signature including a time of erosion
Total duration of complex history	11.4 Ma	LeMasurier and Rex (1989)

[a] References for the chosen values are listed where applicable. All the parameters have been calculated using the equations of Lal (1991) modified by Balco et al. (2008) to include muon production. The models have been calculated using Matlab coding.
[b] Parameters of complex exposure common to all the models.

Table 4
Summary of the minimum amount of material removed and maximum erosion rates (ε) required to generate the cosmogenic ^{3}He—^{10}Be signatures; the total material removed over 11.4 Ma and the minimum number of events necessary to remove this material has been calculated (uncertainties are reported as 1σ).

Sample name	Material removed in one event (m)	±	ε (m/Ma) over 11.4 Ma	±	Total material removed (m)	±	N. events	±
MH.1	0.82	0.07	0.32	0.03	3.65	0.34	4.4	0.6
MH.2	1.43	0.11	0.33	0.03	3.76	0.34	2.6	0.3
MB.71.7	2.62	0.21	0.32	0.03	3.65	0.34	1.4	0.2
MB.71.8	1.23	0.10	0.49	0.04	5.59	0.46	4.5	0.5
MB.71.9	1.45	0.12	0.20	0.02	2.28	0.23	1.6	0.2
MB.71.10	2.4	0.19	0.71	0.06	8.09	0.68	3.4	0.4

Erosion rate increases mainly occur during changes from periods of stability to times of frequent abrupt changes in temperature and precipitation that break the landscape equilibrium (Peizhen et al., 2001). Since the late Miocene several glacial-interglacial cycles have been responsible for fluctuations in the climatic conditions in Antarctica that might have resulted in episodic erosion rate changes that average out into low long-term erosion rates that are typical of the region. The multiple erosional pulses required in model 1 may record major climatic changes such as the transition from cool to warmer climatic conditions during the late Pliocene, Quaternary cooling, or middle Pleistocene warming (Pollard and DeConto, 2009). The major Pleistocene erosion pulse tracked in model 2 that brought the xenoliths to the surface may correspond to the transition to cooler climatic conditions during the late Pleistocene (Raymo et al., 2006).

The xenoliths in this study are from a block field of loose volcanic material typical of the exposed mountain tops above the WAIS. Such surfaces are more susceptible to erosion and weathering than those that have experienced ice cover (Sugden et al., 2005) and therefore are more sensitive to the instability generated by changing climate. Physical rock weathering is responsible for rock mass loss under wet or dry conditions in the case of the extreme low Antarctic temperatures (Elliott, 2008). Andrews and LeMasurier (1973) observed water accumulation produced by local snowmelt during the Antarctic summers. This could be responsible for local freeze-thaw type erosion, which would comminute rock slabs with consequent increase in the short-term erosion rates.

7. Conclusions

We have developed a procedure for the extraction and measurement of cosmogenic ^{10}Be from olivine. By combining ^{10}Be with cosmogenic ^{3}He determinations from olivine we can resolve the complexity of long-term landscape development in Antarctica using the volcanic edifices that protrude through the West Antarctic Ice Sheet. Data from mantle xenolith from the summit of Mount Hampton volcano in Marie Byrd Land reveal the episodic erosional history, integrated over an average long-term erosion rate of <1 m/Ma, which is within the range recorded by long-term Antarctica. The data are consistent with an increase of erosion rate, to 2 m/Ma for the last 1.5 Ma or several episodes of erosion that have removed up to ~2.6 m of material over the last 11.4 Ma. Further resolution of the complexity of the erosional history awaits development of other cosmogenic chronometers (e.g., ^{36}Cl).

Our study has empirically demonstrated the episodic nature of surface erosion at a high-latitude, high-elevation site in interior Antarctica and that changes in erosion regime can generate cosmogenic nuclide signatures that plot within the complex exposure area on a two-isotope diagram with no need for cycles of exposure-burial-reexposure. This interpretation is rarely considered when interpreting complex ^{26}Al ^{10}Be—^{21}Ne systematics of Antarctic surfaces. Complex exposure caused by erosion rate variations is a viable alternative explanation for complex exposure-related isotopic signatures and therefore should be considered especially in the cases in which no clear evidence of ice cover is observed. Why and how climate change drove the erosion rate increases is still unclear, but our study strongly suggests that the application of multiple cosmogenic nuclides have a clear potential to trace past environmental or climatic changes in arid regions.

Table 5
Summary of the minimum depth at which samples have been accumulating cosmogenic nuclides and apparent erosion rates (ε) over a maximum time (time of removal) required for generating the cosmogenic ^{3}He—^{10}Be data (uncertainties are reported as 1σ).

Sample name	Depth (m)	±	Time of removal (Ma)	±	Apparent short-term ε (m/Ma)	±
MH.1	1.80	0.14	1.50	0.12	1.20	0.14
MH.2	2.20	0.18	0.50	0.04	4.40	0.50
MB.71.7	3.06	0.24	0.01	0.00	306.00	34.6
MB.71.8	1.60	0.13	0.60	0.05	2.67	0.30
MB.71.9	2.50	0.20	0.50	0.04	5.00	0.57
MB.71.10	3.27	0.26	0.11	0.01	29.70	3.40

Acknowledgements

The PhD of AC was supported by NERC and SUERC. We thank Prof. John Gamble for providing some of the Mount Hampton xenoliths and Dr. Luigia Di Nicola for her valuable assistance in the laboratory and in data interpretation. We also thank the reviewers and the editor for their help improving the manuscript.

References

Ackert, R.P., Barclay, D.J., Borns, H.W., Calkin, P.E., Kurz, M.D., Fastook, J.L., Steig, E.J., 1999. Measurements of past ice sheet elevations in interior West Antarctica. Science 286 (5438), 276–280.
Ackert, R.P., Mukhopadhyay, S., Parizek, B.R., Borns, H.W., 2007. Ice elevation near the West Antarctic Ice Sheet divide during the last glaciation. Geophys. Res. Lett. 34 (21), L21506.
Anderson, J.B., Shipp, S.S., Lowe, A.L., Wellner, J.S., Mosola, A.B., 2002. The Antarctic Ice Sheet during the last Glacial Maximum and its subsequent retreat history: a review. Quat. Sci. Rev. 21 (1), 49–70.
Andrews, J.T., LeMasurier, W.E., 1973. Rates of quaternary glacial erosion and corrie formation, Marie Byrd Land, Antarctica. Geology 1 (2), 75–80.
Balco, G., Shuster, D.L., 2009. ^{26}Al–^{10}Be–^{21}Ne burial dating. Earth Planet. Sci. Lett. 286 (3), 570–575.
Balco, G., Stone, J.O., Lifton, N.A., Dunai, T.J., 2008. A complete and easily accessible means of calculating surface exposure ages or erosion rates from ^{10}Be and ^{26}Al measurements. Quat. Geochronol. 3 (3), 174–195.
Borchers, B., Marrero, S., Balco, G., Caffee, M., Goehring, B., Lifton, N., Stone, J., 2016. Geological calibration of spallation production rates in the CRONUS-Earth project. Quat. Geochronol. 31, 188–198.
Bourlès, D., 1988. Étude de la géochimie de l'isotope cosmogénique ^{10}Be et de son isotope stable ^{9}Be en milieu océanique: application à la datation des sédiments marins. (Ph.D. dissertation). Paris-sud Centre d'Orsay.
Brown, E.T., Brook, E.J., Raisbeckl, G.M., Yioul, F., Kurz, M.D., 1992. ^{10}Be and ^{26}Al in quartz: implications for exposure age dating. Geophys. Res. Lett. 19 (4), 369–372.
Brunsden, D., Thornes, J.B., 1979. Landscape sensitivity and change. Trans. Inst. Br. Geogr. 463–484.
Burnard, P.G., Farley, K.A., 2000. Calibration of pressure-dependent sensitivity and discrimination in Nier-type noble gas ion sources. Geochem. Geophys. Geosyst. 1 (7) (2000GC00038).
Child, D., Elliott, G., Mifsud, C., Smith, A.M., Fink, D., 2000. Sample processing for earth science studies at ANTARES. Nucl. Instrum. Methods Phys. Res., Sect. B 172 (1–4), 856–860.
Chmeleff, J., von Blanckenburg, F., Kossert, K., Jakob, D., 2010. Determination of the ^{10}Be half-life by multi-collector ICP-MS and liquid scintillation counting. Nucl. Instrum. Methods Phys. Res., Sect. B 268 (2), 192–199.
Di Nicola, L., Strasky, S., Schlüchter, C., Salvatore, M.C., Akçar, N., Kubik, P.W., Christl, M., Kasper, H.U., Wieler, R., Baroni, C., 2009. Multiple cosmogenic nuclides document complex Pleistocene exposure history of glacial drifts in Terra Nova Bay (northern Victoria Land, Antarctica). Quat. Res. 71 (1), 83–92.
Di Nicola, L., Baroni, C., Strasky, S., Salvatore, M.C., Schlüchter, C., Akçar, N., Kubik, P.W., Wieler, R., 2012. Multiple cosmogenic nuclides document the stability of the East Antarctic Ice Sheet in northern Victoria Land since the Late Miocene (5–7 Ma). Quat. Sci. Rev. 57, 85–94.
Elliott, C., 2008. Influence of temperature and moisture availability on physical rock weathering along the Victoria Land coast, Antarctica. Antarct. Sci. 20 (1), 61–67.
Foeken, J.P.T., Stuart, F.M., Dobson, K.J., Persano, C., Vilbert, D., 2006. A diode laser system for heating minerals for (U-Th)/He chronometry. Geochem. Geophys. Geosyst. 7, Q04015. https://doi.org/10.1029/2005GC001190.

Goehring, B.M., Kurz, M.D., Balco, G., Schaefer, J.M., Licciardi, J., Lifton, N., 2010. A reevaluation of in situ cosmogenic ^{3}He production rates. Quat. Geochronol. 5 (4), 410–418.
Gosse, J.C., Phillips, F.M., 2001. Terrestrial in situ cosmogenic nuclides: theory and application. Quat. Sci. Rev. 20 (14), 1475–1560.
Hein, A.S., Woodward, J., Marrero, S.M., Dunning, S.A., Freeman, S., Stuart, F.M., Winter, S., Westoby, M.J., Sugden, D.E., 2016. Evidence for dynamic equilibrium of the central divide of the West Antarctic Ice Sheet for 1.4 million years. Nat. Commun. https://doi.org/10.1038/NCOMMS10325.
Kober, F., Ivy-Ochs, S., Schlunegger, F., Baur, H., Kubik, P.W., Wieler, R., 2007. Denudation rates and a topography-driven rainfall threshold in northern Chile: Multiple cosmogenic nuclide data and sediment yield budgets. Geomorphology 83 (1–2), 97–120.
Korschinek, G., Bergmaier, A., Faestermann, T., Gerstmann, U.C., Knie, K., Rugel, G., Kossert, K., 2010. A new value for the half-life of ^{10}Be by heavy-ion elastic recoil detection and liquid scintillation counting. Nucl. Instrum. Methods Phys. Res., Sect. B 268 (2), 187–191.
Kounov, A., Niedermann, S., De Wit, M.J., Viola, G., Andreoli, M., Erzinger, J., 2007. Present denudation rates at selected sections of the South African escarpment and the elevated continental interior based on cosmogenic ^{3}He and ^{21}Ne. S. Afr. J. Geol. 110 (2–3), 235–248.
Lal, D., 1991. Cosmic ray labeling of erosion surfaces: in situ nuclide production rates and erosion models. Earth Planet. Sci. Lett. 104 (2–4), 424–439.
LeMasurier, W.E., 1987. Mount Hampton. Volcanoes of the Antarctic Plate and Southern Oceans, pp. 189–194.
Lemasurier, W.E., Kawachi, Y., 1990. Mount Hampton. In: LeMasurier, W.E., Thomson, J.W. (Eds.), Volcanoes of the Antarctic Plate and Southern Oceans. American Geophysical Union, Antarctic Research Series vol. 48, pp. 189–194.
LeMasurier, W.E., Rex, D.C., 1989. Evolution of linear volcanic ranges in Marie Byrd Land, West Antarctica. J. Geophys. Res. Solid Earth 94 (B6), 7223–7236.
LeMasurier, W.E., Rocchi, S., 2005. Terrestrial record of post-Eocene climate history in Marie Byrd Land, West Antarctica. Geogr. Ann. Ser. A. Phys. Geogr. 51–66.
LeMasurier, W.E., Thomson, J.W. Eds, 1990. Volcanoes of the Antarctic plate and southern oceans. American Geophysical Union, Antarctic Research Series. vol. 48 (487 pp.).
LeMasurier, W.E., Futa, K., Hole, M., Kawachi, Y., 2003. Polybaric evolution of phonolite, trachyte, and rhyolite volcanoes in eastern Marie Byrd Land, Antarctica: controls on peralkalinity and silica saturation. Int. Geol. Rev. 45 (12), 1055–1099.
Mabry, J., Burnard, P., Blard, P.H., Zimmermann, L., 2012. Mapping changes in helium sensitivity and peak shape for varying parameters of a Nier-type noble gas ion source. J. Anal. At. Spectrom. 27 (6), 1012–1017.
Margerison, H.R., Phillips, W.M., Stuart, F.M., Sugden, D.E., 2005. An assessment of cosmogenic ^{3}He surface exposure dating in the Northern Dry Valleys of East Antarctica. Earth Planet. Sci. Lett. 230, 163–175.
Marrero, S.M., Phillips, F.M., Borchers, B., Lifton, N., Aumer, R., Balco, G., 2016. Cosmogenic nuclide systematics and the CRONUScalc program. Quat. Geochronol. 31, 160–187.
Marrero, S.M., Hein, A.S., Naylor, M., Attal, M., Shanks, R., Winter, K., Sugden, D., 2018. Controls on subaerial erosion rates in Antarctica. Earth Planet. Sci. Lett. 501, 56–66.
Masarik, J., 2002. Numerical simulation of in situ production of cosmogenic nuclides. Geochim. Cosmochim. Acta 66 (15A), A491.
Matsuda, J., Matsumoto, T., Sumino, H., Nagao, K., Yamamoto, J., Miura, Y., Kaneoka, I., Takahata, N., Sano, Y., 2002. The ^{3}He/^{4}He ratio of the new internal He Standard of Japan (HESJ). Geochem. J. 36 (2), 191–195.
Middleton, J.L., Ackert, R.P., Mukhopadhyay, S., 2012. Pothole and channel system formation in the McMurdo Dry Valleys of Antarctica: new insights from cosmogenic nuclides. Earth Planet. Sci. Lett. 355, 341–350.
Mukhopadhyay, S., Ackert, R.P., Pope, A.E., Pollard, D., DeConto, R.M., 2012. Miocene to recent ice elevation variations from the interior of the West Antarctic ice sheet: Constraints from geologic observations, cosmogenic nuclides and ice sheet modeling. Earth Planet. Sci. Lett. 337, 243–251.
Nicolas, J.P., Bromwich, D.H., 2014. New reconstruction of Antarctic near-surface temperatures: Multidecadal trends and reliability of global reanalyses. J. Clim. 27 (21), 8070–8093.
Nishiizumi, K., Kohl, C.P., Arnold, J.R., Klein, J., Fink, D., Middleton, R., 1991. Cosmic ray produced ^{10}Be and ^{26}Al in Antarctic rocks: exposure and erosion history. Earth Planet. Sci. Lett. 104 (2–4), 440–454.
Oberholzer, P., Baroni, C., Schaefer, J.M., Orombelli, G., Ochs, S.I., Kubik, P.W., Baur, H., Wieler, R., 2003. Limited Pliocene/Pleistocene glaciation in Deep Freeze Range, northern Victoria Land, Antarctica, derived from in situ cosmogenic nuclides. Antarct. Sci. 15 (04), 493–502.
Panter, K.S., Hart, S.R., Kyle, P., Blusztanjn, J., Wilch, T., 2000. Geochemistry of Late Cenozoic basalts from the Crary Mountains: characterization of mantle sources in Marie Byrd Land, Antarctica. Chem. Geol. 165 (3), 215–241.
Parai, R., Mukhopadhyay, S., Lassiter, J.C., 2009. New constraints on the HIMU mantle from neon and helium isotopic compositions of basalts from the Cook–Austral Islands. Earth Planet. Sci. Lett. 277 (1), 253–261.
Paulsen, T.S., Wilson, T.J., 2010. Evolution of Neogene volcanism and stress patterns in the glaciated West Antarctic Rift, Marie Byrd Land, Antarctica. J. Geol. Soc. 167 (2), 401–416.
Peizhen, Z., Molnar, P., Downs, W.R., 2001. Increased sedimentation rates and grain sizes 2–4 My ago due to the influence of climate change on erosion rates. Nature 410 (6831), 891.
Placzek, C.J., Matmon, A., Granger, D.E., Quade, J., Niedermann, S., 2010. Evidence for active landscape evolution in the hyperarid Atacama from multiple terrestrial cosmogenic nuclides. Earth Planet. Sci. Lett. 295 (1–2), 12–20.
Pollard, D., DeConto, R.M., 2009. Modelling West Antarctic ice sheet growth and collapse through the past five million years. Nature 458 (7236), 329.
Raymo, M.E., Lisiecki, L.E., Nisancioglu, K.H., 2006. Plio-Pleistocene ice volume, Antarctic climate, and the global δ18O record. Science 313 (5786), 492–495.
Rocchi, S., LeMasurier, W.E., Di Vincenzo, G., 2006. Oligocene to Holocene erosion and glacial history in Marie Byrd Land, West Antarctica, inferred from exhumation of the Dorrel Rock intrusive complex and from volcano morphologies. Geol. Soc. Am. Bull. 118 (7–8), 991–1005.
Ryan, J.G., Kyle, P.R., 2004. Lithium abundance and lithium isotope variations in mantle sources: insights from intraplate volcanic rocks from Ross Island and Marie Byrd Land (Antarctica) and other oceanic islands. Chem. Geol. 212 (1), 125–142.
Seidl, M.A., 1993. Form and Process in Channel Incision of Bedrock. (PhD dissertation). University of California, Berkeley.
Seidl, M.A., Finkel, R.C., Caffee, M.W., Hudson, G.B., Dietrich, W.E., 1997. Cosmetic isotope analyses applied to river longitudinal profile evolution: problems and interpretations. Earth Surf. Process. Landf. 22 (3), 195–209.
Seitz, H.M., Brey, G.P., Lahaye, Y., Durali, S., Weyer, S., 2004. Lithium isotopic signatures of peridotite xenoliths and isotopic fractionation at high temperature between olivine and pyroxenes. Chem. Geol. 212 (1–2), 163–177.
Steig, E.J., Fastook, J.L., Zweck, C., Goodwin, I.D., Licht, K.J., White, J.W., Ackert, R.P., 2001. West Antarctic ice sheet elevation changes. The West Antarctic Ice Sheet: Behavior and Environment, pp. 75–90.
Stone, J.O., 2000. Air pressure and cosmogenic isotope production. J. Geophys. Res. Solid Earth 105 (B10), 23,753–23,759.
Stone, J.O., Balco, G.A., Sugden, D.E., Caffee, M.W., Sass, L.C., Cowdery, S.G., Siddoway, C., 2003. Holocene deglaciation of Marie Byrd land, west Antarctica. Science 299 (5603), 99–102.
Stuart, F.M., Burnard, P.G., Taylor, R., Turner, G., 1995. Resolving mantle and crustal contributions to ancient hydrothermal fluids: He-Ar isotopes in fluid inclusions from Dae Hwa W-Mo mineralisation, South Korea. Geochim. Cosmochim. Acta 59 (22), 4663–4673.
Stuart, F.M., Lass-Evans, S., Fitton, J.G., Ellam, R.M., 2003. High ^{3}He/^{4}He ratios in picritic basalts from Baffin Island and the role of a mixed reservoir in mantle plumes. Nature 424 (6944), 57–59.
Sugden, D.E., Balco, G., Cowdery, S.G., Stone, J.O., Sass, L.C., 2005. Selective glacial erosion and weathering zones in the coastal mountains of Marie Byrd Land, Antarctica. Geomorphology 67 (3), 317–334.
Sugden, D.E., Hein, A.S., Woodward, J., Marrero, S.M., Rodés, A., Dunning, S.M., Stuart, F.M., Freeman, S., Winter, K., Westoby, M.J., 2017. The million-year evolution of the glacial trimline in the southernmost Ellsworth Mountains, Antarctica. Earth Planet. Sci. Lett. 469, 42–52.
Tabushi, M., 1958. Solvent extraction of beryllium as acetylacetonate. Bull. Inst. Chem. Res., Kyoto Univ. 36 (6), 156–162.
Van der Wateren, F.M., Dunai, T.J., Van Balen, R.T., Klas, W., Verbers, A.L., Passchier, S., Herpers, U., 1999. Contrasting Neogene denudation histories of different structural regions in the Transantarctic Mountains rift flank constrained by cosmogenic isotope measurements. Glob. Planet. Chang. 23 (1), 145–172.
Williams, A.J., Stuart, F.M., Day, S.J., Phillips, W.M., 2005. Timing and rate of landscape development in central Gran Canaria, eastern Atlantic Ocean, from cosmogenic ^{3}He concentrations in pyroxene microphenocrysts. Quat. Sci. Rev. 24, 211–222.
Wysoczanski, R.J., Gamble, J.A., Kyle, P.R., Thirlwall, M.F., 1995. The petrology of lower crustal xenoliths from the Executive Committee Range, Marie Byrd Land volcanic province, West Antarctica. Lithos 36 (3–4), 185–201.
Xu, S., Dougans, A.B., Freeman, S.P., Schnabel, C., Wilcken, K.M., 2010. Improved ^{10}Be and ^{26}Al-AMS with a 5 MV spectrometer. Nucl. Instrum. Methods Phys. Res., Sect. B 268 (7–8), 736–738.